MATER. RES. LETT.
https://doi.org/10.1080/21663831.2024.2421867

MATERIALS RESEARCH LETTERS
Taylor & Francis
Taylor & Francis Group

ORIGINAL REPORT

Compressive behavior and connecting topology of monolithic nanoporous niobium

Seoyun Sohn[a,b], Shan Shi[a,c], Jürgen Markmann[a,b], Stefan Alexander Berger[a] and Jörg Weissmüller[a,b]

[a]Institute of Hydrogen Technology, Helmholtz-Zentrum Hereon, Geesthacht, Germany; [b]Institute of Materials Physics and Technology, Hamburg University of Technology, Hamburg, Germany; [c]Research Group of Integrated Metallic Nanomaterials Systems, Hamburg University of Technology, Hamburg, Germany

ABSTRACT

With an eye on the role of structure size and topology, this study explores the mechanical behavior of nanoporous (NP) Nb made by liquid-metal dealloying. Results from X-ray nanotomography and macro-compression tests confirm that coarsening degrades the yield strength and that Young's modulus deviates from scaling laws developed for NP Au made by dealloying in aqueous media. We find that the scaled genus of NP Nb is lower than what has been reported for NP Au, and this low connectivity provides an obvious explanation for the low modulus. Furthermore, the structural dispersion implies that additional structural descriptors should be acknowledged.

IMPACT STATEMENT

Jointly considering mechanical tests and tomographic reconstruction for nanoporous Nb made by liquid-metal dealloying reveals substantial differences to materials made by conventional aqueous dealloying; this results from lesser structural order.

ARTICLE HISTORY
Received 11 July 2024

KEYWORDS
Dealloying; nanoporous; niobium; mechanical behavior; tomography

1. Introduction

Studying the mechanical performance of nano- and microscale porous materials allows us to understand small-scale solids and to enhance their materials design for functional applications [1]. Such materials with a bicontinuous network structure have previously demonstrated potential as light-weight structural materials [2], catalysts [3,4], actuators [5–7], semiconductor interconnects [8] and sensors [9–12]; they have also demonstrated recoverable tuning of mechanical properties [13] and even enhanced radiation resistance [14]. As load-bearing capability is typically a prerequisite for operation as a functional material, the mechanical behavior of nano- and microporous metals have been intensely investigated, using testing schemes both at the macro- [15–20] and at the microscale [21–25]. Most studies have been confined to noble metals such as gold [15,26], silver [27,28], palladium [5,6], or platinum [29], since their high electronegativity facilitates preparation by (electro)chemical dealloying in aqueous media.

Aqueous dealloying involves the selective dissolution of less noble constituent(s) in an electrolyte; the remaining more noble constituent rearranges to form a bicontinuous porous structure. By contrast, liquid metal dealloying (LMD) relies on differences in enthalpy of mixing for dissolution selectivity [30,31], thereby expanding the materials scope. Over the last decade, porous materials composed of less-costly materials such as Ti [32] and its alloys [33], FeCr [34,35], Nb [36], stainless steel [37] and high-entropy alloys [38] have been made using LMD. Numerical simulation [39–41] and experimental 3D characterization have studied the morphological and chemical evolution [37,42] during LMD.

While both dealloying techniques, electrochemical and liquid-metal dealloying, rely on similar microstructural evolution processes, structural differences in the product material have been noticed. The most obvious is the coarser microstructures generated by LMD. Furthermore, LMD features elongated ligaments in the dealloying front, a phenomenon not previously observed in aqueous dealloying [37]. Despite these differences, explanatory approaches to the mechanical behavior have invoked similar concepts. For instance, strength and elasticity relations of LMD-made porous FeCr is well com-

CONTACT Seoyun Sohn seoyun.sohn@hereon.de Institute of Hydrogen Technology, Helmholtz-Zentrum Hereon, Geesthacht 21502, Germany; Institute of Materials Physics and Technology, Hamburg University of Technology, Hamburg 21073, Germany

Supplemental data for this article can be accessed online at http://dx.doi.org/10.1080/21663831.2024.2421867.

patible with the Gibson-Ashby scaling equations [34], which–in modified form–also provide a basis for the mechanics of electrochemically dealloyed nanoporous gold [43]. Yet, it remains to be explored how details of the microstructural morphology or topology of LMD porous solids connect to their mechanical properties. The present study addresses that issue.

Porous Nb, created by removing Ni from Nb-Ni in an Mg melt, has been the subject of several studies, particularly for possible application in supercapacitors [36,44,45]. Using that system, we study mechanical properties in dependence of ligament size and solid fraction, alongside 3D microstructure reconstructions. We show that the elastic behavior of NP Nb differs significantly from that of electrochemically dealloyed NP Au, which is the benchmark for dealloyed nanoporous metals. The difference is attributed to structural connectivity. This suggests that porous structures produced through LMD may exhibit notable distinctions from structures made by (electro)chemical dealloying, such as NP Au.

2. Procedures

2.1. Liquid-metal dealloying

The $Nb_{25}Ni_{75}$ (at%) precursor alloy was prepared by repeatedly melting and solidifying high-purity Nb (99.96%) and Ni (99.99+%) wires in an arc melter. The ingot was annealed under Argon gas flow for 12 hours at 1200°C and furnace cooled. A circular disk was cut and then ground to 2500 grade finish using a guiding die. This established smooth and coplanar surfaces for later loading in the testing device. Cuboids with edge length 1.0 ± 0.2 mm were then cut with a diamond wire saw, thereby establishing the free side surfaces.

Liquid metal dealloying was performed on $Nb_{25}Ni_{75}$ cuboids in Mg melt at a temperature fixed between 800 and 900°C. Precursor samples, covered with $\sim$100 mg of Mg (as granules, $-20 + 100$ mesh, 99.8% metal basis), were placed in a Sigradur G glassy carbon crucible (GAT 007, HTW Hochtemperatur-Werkstoffe GmbH) of volume 0.07 mL and heated in an infrared furnace, under Argon flow and with a heating rate of 50°C/s. Dealloying times ranged from 30 to 90 minutes. After dealloying, excess Mg mixed with Ni was etched with 3 M nitric acid for >12 hours, then the sample was rinsed with first ultrapure water (Arium Comfort I TOC, Sartorius) and then ethanol and air-dried.

2.2. Structural and phase characterization

The solid volume fraction, φ, of the nanoporous sample was determined from mass and volume, with volume obtained from edge lengths measured with an optical microscope (SZX10, Olympus). Characterization by wide-angle X-ray diffraction used a powder diffractometer (D8 Advance, Bruker AXS) in focusing Bragg-Brentano geometry, with Mo K_α radiation and an energy dispersive, position sensitive detector (LynxEye XE-T). Energy dispersive X-ray spectroscopy in the Scanning Electron Microscope (SEM, Zeiss Supra VP55) used a silicon drift detector (Oxford Instruments).

The ligament sizes in electron micrographs were acquired using the Python package AQUAMI [46]. Micrographs were first captured at ×10 k magnification for each sample's fracture surfaces as representative of the bulk, and the neck diameters of the ligaments and their distribution were observed based on the SEM images. At least 300 diameter values were acquired to calculate the mean ligament size, L, and the variance, s, of the size distribution. The bootstrap error is quoted as a measure for the uncertainty of L [47].

2.3. Mechanical characterization

The samples for mechanical tests were $\sim 1 \times 1 \times 1\,\mathrm{mm}^3$ cuboids. Using a conventional testing device (Z010, ZwickRoell equipped with a laser speckle extensometer system, LaserXtens, for strain measurement), we conducted uniaxial compression tests at room temperature. For assuring good contact to the load surfaces, the sample position was optimized using the camera feed of the laser speckle extensometer system and a 2 N preload applied. Stress-strain response was recorded with an engineering strain rate of $10^{-4}\,\mathrm{s}^{-1}$ and unload steps after each 2.5×10^{-2} strain increment. Each unloading step terminated at 1 MPa and was followed by immediate reloading.

2.4. Tomographic reconstruction

X-ray nanotomography sample preparation used a Xe plasma focused ion beam (Helios G4 UXe, Thermoscientific). A freestanding cuboid was cut first and then milled to a cylindrical micropillar. The ion beam was initially directed normal to the pillar axis to lathe mill the sample, with an accelerating voltage of 30 kV and beam currents of 2.5 and then 1 μA.

Next, beam currents of 4 and then 1 nA were applied, directed from the top. The low second beam current prevents 'curtaining' and minimizes energy intake to the pillar surface. Their size, 50 μm in diameter and 88 μm in height, relative to the ligament size makes the resulting columns representative samples of the microstructure [48]. Due to their large diameters, FIB damage in the bulk of the pillars may be excluded.

The tomography measurement in a Zeiss Xradia 800 Ultra used monochromatic Cu K_α radiation and a large field of view (LFOV) imaging mode with cross-sectional

images taken from an 180° arc. Since the height of the micropillar is larger than the field of view of 65 μm × 65 μm, two successive measurements were performed for each micropillar and the two sets of images were stitched using ImageJ [49].

The images were binarized into solid and pore via the Otsu thresholding algorithm [50] integrated in ImageJ, with a threshold matching the solid fraction to the value independently determined from mass per volume.

The binarized reconstruction formed the basis for determining the topological genus, G, with the software plugin BoneJ in ImageJ [51–53]. The scaled genus, g_V, provides a characteristic of the topology that is independent of the sample size and of the characteristic microstructural length scale. It is defined by

$$g_V = \frac{G}{V}\tilde{L}^3 \tag{1}$$

where V is the total volume (solid plus pores) and $\tilde{L}$ is the mean spacing between neighboring ligaments.

For use in Equation (1), we determined $\tilde{L}$ from the area of surface in the reconstruction, as measured by evaluating the surface mesh with Simpleware ScanIP (Simpleware Product Group, Bradninch Hall, United Kingdom). Specifically, we used the relation between $\tilde{L}$ and the surface area-to-volume ratio, S, of leveled-wave structures. Those structures provide a geometric model approximating dealloyed nanoporous solids [54]; they are characterized by

$$S = \frac{2q_0}{\pi\sqrt{3}}e^{-\xi^2/2} \tag{2}$$

with q_0 the magnitude of a characteristic wave vector and ξ defined as

$$\xi = -\sqrt{2}\,\mathrm{erf}^{-1}(2\varphi - 1)\,. \tag{3}$$

We solved Equation (2) for q_0 and then obtained $\tilde{L}$ as

$$\tilde{L} = \alpha\frac{2\pi}{q_0}, \tag{4}$$

where α is a numerical constant, $\alpha = 1.23$ [54].

3. Results

3.1. Microstructure

Porous samples were dealloyed in a liquid Mg bath from $Nb_{25}Ni_{75}$ precursor. X-ray diffraction Figure 1(a) shows peaks attributed to orthorhombic $NbNi_3$ in the precursor alloy. The x-ray powder diffractogramm from a fracture surface, Figure 1(b), confirms complete through-bulk dealloying with predominant body-centered cubic Nb

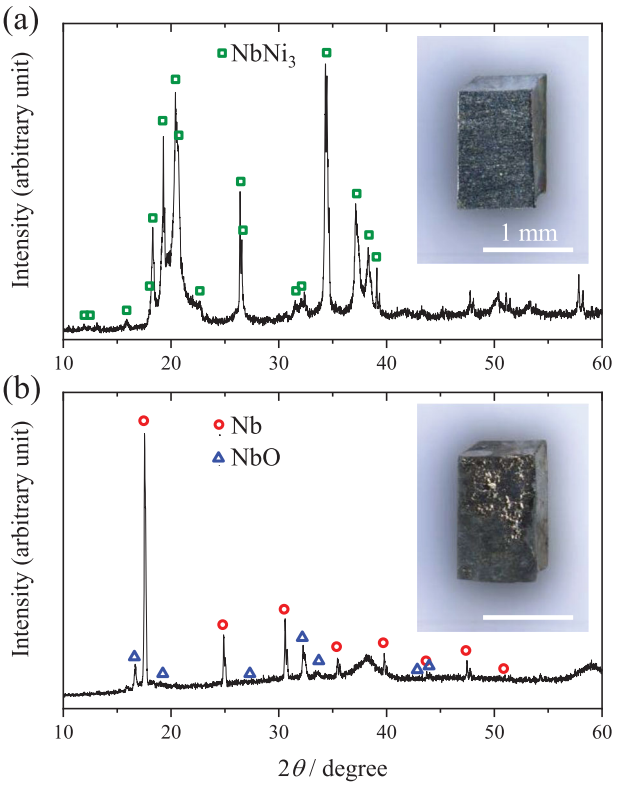

Figure 1. X-ray diffraction patterns and optical images of (a) a precursor alloy with a nominal composition of $Nb_{25}Ni_{75}$ (at%) and (b) nanoporous Nb prepared by liquid metal dealloying at 850°C for 45 minutes. Markers indicate reflection positions of reference patterns for various crystal structures, see legends.

phase. The diffractogram shows weak reflections of NbO, an oxide species commonly formed when Nb is exposed to atmosphere [55].

The optical appearance of each sample is shown in the insets of Figure 1. Nanoporous Nb retains the precursor's geometry, with no visible macroscopic cracks or shrinkage observed under the microscope, consistently reproduced in this study. The EDX analysis finds 99.2 ± 0.7 at% Nb in the dealloyed sample; residual Mg and Ni were < 0.1 at% and 0.8 ± 0.8 at%, respectively.

Figure 2 shows the SEM images of NP Nb prepared under nine different dealloying conditions. For representative cross-sectional micrographs, the samples were sliced using a scalpel and their cross-sections were observed. Each sample is composed of a bicontinuous network of randomly oriented Nb ligaments. The ligament size and morphology showed no visible differences between the center and near-surface areas of the cross-sections. (see SI, Figure S1) The solid volume fraction of each of the nine samples tested is 0.36.

Ligament sizes were determined from SEM micrographs, measuring ligament diameters near their center as exemplified by the arrow in Figure 2. The mean ligament size, L, of individual samples ranges from a few

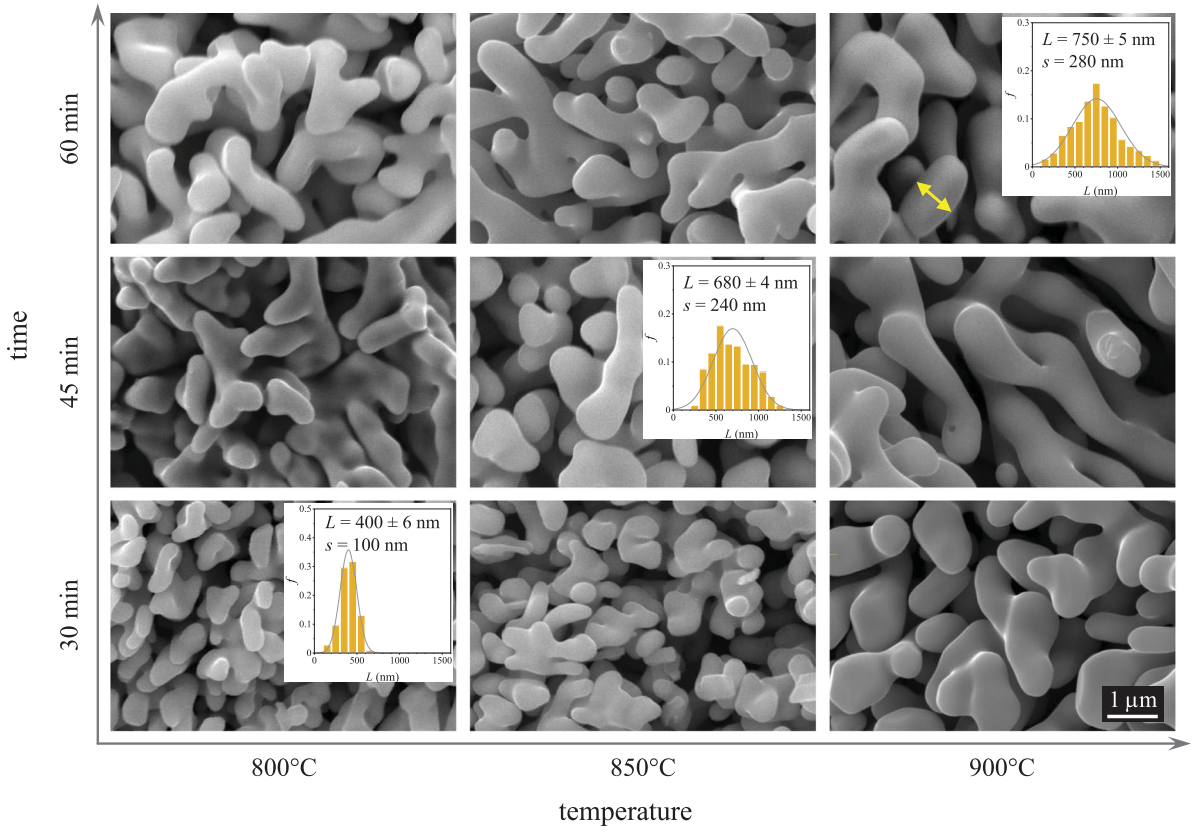

Figure 2. Scanning electron micrographs of nanoporous Nb dealloyed under nine different combinations of immersion time (see ordinate) and temperature (see abscissa) conditions. Insets show ligament size distribution histograms for selected conditions. L is the mean ligament size and s its standard deviation.

hundred nm to $> 1\,\mu$m, depending on the dealloying condition. Note the distinction between L and the mean ligament spacing, $\tilde{L}$, discussed in Section 2.4. A noticeable trend can be seen when comparing the dealloying conditions presented in Figure 2: smaller ligaments are produced at lower dealloying temperature and/or with shorter immersion time. As an example for sample-to-sample variation, the L of six samples prepared at 850°C for 30 minutes, including the one in Figure 2, was 380 ± 60 nm.

3.2. Mechanical properties under compression

Figure 3(a) shows stress-strain graphs in compression, displayed as engineering stress, σ_{eng}, versus engineering strain, ε_{eng}. The graphs are from individual samples, prepared under three different dealloying conditions: 850°C for 30 minutes, 900°C for 60 minutes and 900°C for 90 minutes, resulting in average ligament sizes of 320 ± 2, 690 ± 4 and 840 ± 3 nm with standard deviations the ligament size distribution at 130, 320 and 420 nm, respectively. Consistent results were obtained in mechanical tests of two or three samples for each quality, and representative findings are shown below.

The effective Young's modulus, E, in different states of compression was determined as the secant modulus from the unload-reload segments in Figure 3(a). Figure 4 shows the φ-dependence of E of NP Nb scaled by the Young's modulus of massive Nb, $E_s = 103$ GPa [56]. As compression progresses, the solid fraction increases with plastic strain. Figure 4 reflects this trend, where higher E is observed with larger φ. Across the data groups for different ligament sizes in Figure 4, the size dependency of E is weak.

Figure 3(b–c) displays the structural change at $\varepsilon_{\text{eng}} = 0.4$ compared to the relaxed (as-dealloyed) network. The ligament spacing decreases, aligning with the expected outcome of plastic compression forming new contacts between neighboring ligaments. Mechanical failure occurred once the strain exceeded 0.4.

3.3. Scaled genus

Figure 5(a) shows an SEM image of a micro-pillar for X-ray nanotomography. The porous structure is visible at the FIB-milled surface of the sample. Four samples were investigated, with their dealloying conditions and $\tilde{L}$ values listed in Table 1.

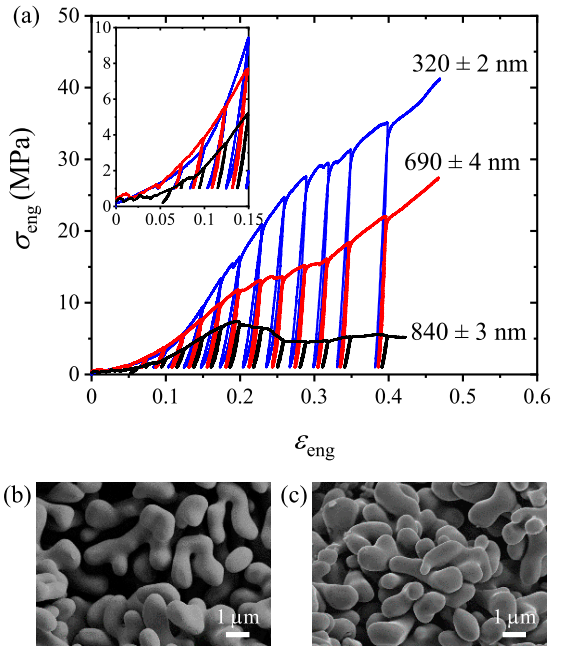

Figure 3. (a) Stress-strain curves of NP Nb samples with three different mean ligament sizes. The inset shows the curves at the low strain level. SEM images of NP Nb with (b) $\varepsilon_{eng} = 0$ and (c) $\varepsilon_{eng} = 0.4$ of compression. In (b) and (c), the NP Nb is dealloyed at 900°C for 90 minutes.

Figure 5(b) is the binarized reconstruction of the micro-pillar in Figure 5(a). The porous structure closely resembles that seen in the SEM image. For further analysis, a $>1\,\mu$m outer surface layer is cropped out. This minimizes any effects arising from the FIB-curtained surface, while the column volume remains sufficient to be representative.

Table 1. Dealloying conditions and the mean ligament spacing, $\tilde{L}$, determined by X-ray nanotomography. T is the temperature of Mg melt and t is the immersion time.

T (°C)	t (min)	$\tilde{L}$ (μm)
800	45	1.46
850	30	1.52
850	30	1.76
900	60	1.37

The scaled genera obtained from the experimental tomographic reconstructions are displayed in Figure 5(c), with the $\varphi - g_V$ relation [54] for the leveled-wave model superimposed for comparison. Figure 5(d) complements that graph with a display of g_V versus $\tilde{L}$. It is seen that our sample set explores essentially a single φ value and a quite narrow range of $\tilde{L}$. This prevents substantiated conclusions on how g_V correlates with those parameters. For further discussion, we consider only the average value, $\bar{g}_V$.

We find $\bar{g}_V = 1.21 \pm 0.15$ from the set of samples listed in Table 1. As compared to the leveled-wave model at the same solid fraction, the $\bar{g}_V$ of NP Nb is less by the factor ~ 1.5. Since the leveled wave model is considered as an adequate description of NP Au, we are led to conclude that the network structure of NP Nb is less connected than that of NP Au.

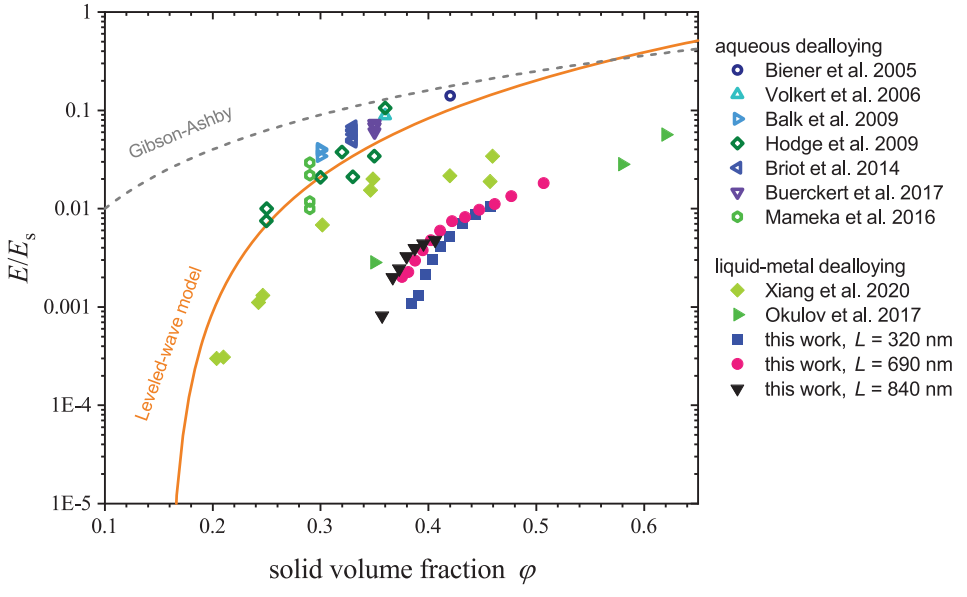

Figure 4. Scaled Young's modulus of nanoporous Nb (this work) and other reported porous materials produced by liquid-metal dealloying [32,34] (closed symbols), and of nanoporous Au produced by aqueous dealloying [18,21,57–61] (open symbols). All data points are scaled by the Young's modulus of base material, E_s. The modified Roberts-Garboczi scaling law for the leveled wave model [54] and Gibson-Ashby scaling law [62] are displayed for reference.

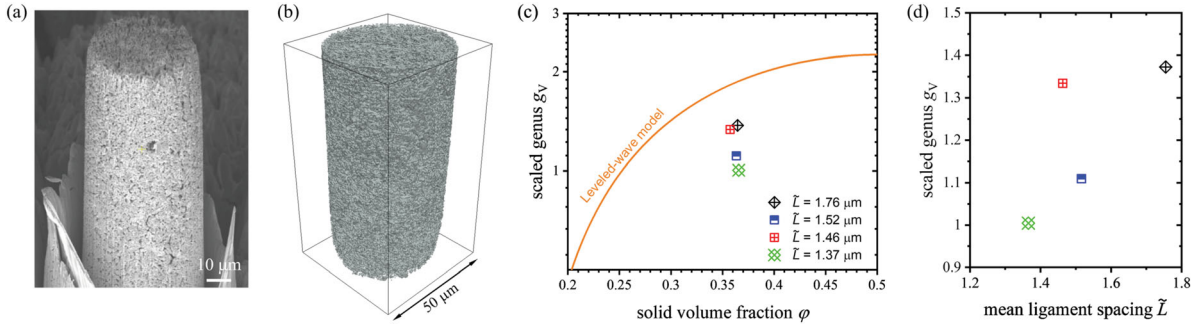

Figure 5. (a) SEM image of an NP Nb micropillar and (b) its X-ray nanotomography-based 3D reconstruction. Note that the sample has been rotated by an arbitrary angle, providing a different perspective from (a). (c) Scaled genus, g_V, versus solid fraction, φ. A skin layer–possibly FIB-affected–has been removed for the g_V calculation. Solid line: leveled-wave model [54] (d) g_V versus the mean ligament spacing, $\tilde{L}$, of the four NP Nb micropillars.

4. Discussion

4.1. Mean ligament size and size distribution

It has been suggested that L, the characteristic length scale of an LMD structure, is determined primarily by the coarsening kinetics, and that those obey the power law $L \propto \sqrt{d}$ where d is the dealloyed depth [39]. That would suggest a gradient in ligament size as one moves from the outer surface into the interior of a sample. A more recent investigation, on the other hand, has pointed out that–at sufficiently high temperature–the local dealloying direction may diverge from that of the macroscopic sample surface normal [63]. This implies that an appropriate notion of d can differ locally within the sample. Irrespective of the different suggestions, our electron micrographs did not reveal a noticeable dependency of L on the distance from the sample's exterior surface, indicating each sample has a uniform mean ligament size L.

Figure 2 demonstrates that the L of individual samples can be controlled by adjusting the immersion time and the temperature of molten Mg. As mentioned earlier in Section 3.1, higher temperature and longer immersion time result in larger L, confirming the coarsening trend reported in [45].

It is also noteworthy that the coefficient of variation, defined as the ratio of the standard deviation, s, to the mean ligament size, L, increases with L. For the examples in Figure 2 we find $s/L = 0.25$, 0.35 and 0.37 in order of ascending L. For electrochemically dealloyed NP Au, experiment suggests $s/L = 0.303 \pm 0.007$ throughout an interval of ligament size including 20-fold coarsening [47]. This is consistent with self-similar microstructure evolution in NP Au. Self similarity is also implied by experimental topology analysis of coarsened NP Au [48] and by atomistic simulation [64] of coarsening for $\varphi > 0.3$, as in the present samples. While the absolute s/L values for NP Nb—coarsened in-situ during LMD—are roughly similar to NP Au, s/L of NP Nb systematically increases with $\tilde{L}$, suggesting a gradual loss of structural order and, hence, non-self-similar coarsening. This is consistent with previous findings for LMD-generated porous metals [37]. To summarize, our NP Nb samples are distinguished from NP Au by their reduced microstructural order, their non-self-similar coarsening, and their lesser scaled genus.

Investigations into the mechanism of LMD have emphasized the distinction to aqueous-solution dealloying (ASD), and specifically a strong variability of the microstructural morphologies generated by LMD [39,40]. Whereas ASD is controlled sensibly by the kinetics of dissolution and of surface diffusion alone, the transport in the melt and the ensuing phenomena of variable dissolution rate and repartitioning of the master alloy's constituents may generate a richer set of morphologies for LMD. This aligns with morphological variation during coarsening and, hence, a reduced order.

Besides their different transport pathways, LMD and ASD are also distinguished by their microstructure evolution sequences and by the magnitude of the acting driving force for coarsening. ASD proceeds by primary and then secondary dealloying, the former establishing the initial network in response to the driving force for dissolution while the latter coarsens the network in response to driving forces from capillarity [65,66]. There are observations where the primary dealloyed network is quite disordered, yet coarsening transforms it to a spinodal-like, ordered network structure [67]. The primary/secondary dealloying distinction has not been reported for LMD [39,68], suggesting that the ordering tendency of coarsening acts less prominently there. The coarsening behavior of nanoporous metals, which generates and maintains spinodal-like structures–and often

self-similarity–is understood as the result of two governing factors, capillarity as the driving force and diffusion as the transport mechanism [64,69]. As it scales with the product of surface tension and mean curvature, capillarity is strong in ASD materials with truly nanoscale ligament size. Yet, LMD generates micron-scale structures, where the mean curvature can be orders of magnitude weaker. Other factors, for instance crystal lattice defects or microstrain, may then become significant and interfere with the ordering tendency of diffusive coarsening. This may contribute to the deviation, in LMD porous metals, from the well-defined, spinodal-like structures of ASD metals.

4.2. Young's modulus and connectivity

We found no obvious dependence of E on the ligament size. A size-dependency may arise from the surface excess elasticity, yet this becomes appreciable only at structure sizes significantly below 10 nm [70,71]. Thus, our results relate to a scale-independent elasticity regime where network topology may be decisive [43,71,72].

The effective Young's modulus of NP Nb is plotted in Figure 4 alongside LMD-made porous Ti and $Fe_{0.80}Cr_{0.20}$ [32,34] and NP Au (aqueous dealloying) [18,21,57–61]. The Gibson-Ashby scaling law [62] and the modified Roberts-Garboczi scaling law parameterized for NP Au and for leveled-wave structures [54] are superimposed for comparison.

The modified Roberts-Garboczi scaling law fitted to the leveled-wave structure has successfully reproduced the relation between microstructural features and elastic properties of NP Au [54] as shown in the Figure. Strikingly, NP Nb exhibits a 10 to 60 times lower modulus compared to the scaling laws. E is also considerably lower than the experimental results for NP Au of similar relative density [21,43,73]. This anomalous compliance indicates that the Gibson-Ashby scaling law overpredicts NP Nb's stiffness from its φ, and the fitting parameters of the Roberts-Garboczi scaling law for NP Au might not be applicable to NP Nb.

Deviations between the Gibson-Ashby scaling for constant-connectivity structures and real NP materials have been related to a solid-fraction dependent connectivity [20,43,61,74–77]. This motivates our examination of the topological genus, as a quantifiable measure for connectivity. We find the average g_V of NP Nb at 1.2 and, thereby, $\sim$1.5 times less than that [54] of the leveled-wave model structure at the same solid fraction. Qualitatively, therefore, the anomalous compliance of NP Nb can be traced back to its deficiency in connectivity. For network structures derived from the leveled-wave model but with disconnections due to coarsening, the E at any given solid fraction scales as g_V^2 [77]. That scaling is obviously not applicable to our LMD Nb samples since – compared to NP Au—NP Nb's reduction in E considerably exceeds the squared relative change in scaled genus. This emphasizes further that the microstructural morphology and topology of the LMD samples differ substantially from that of NP Au made by aqueous dealloying.

When it comes to microstructure metrics for nano porous metals that might impact their mechanics, on top of the classic parameters solid fraction and ligament size, the topological genus stands out because its link to stiffness and strength has been firmly established [2,43,54,61,76] and–for the special case of spinodal-like structures–cast into a scaling law [77]. Yet, other metrics have also been suggested or revealed as relevant. Besides the above-mentioned width of the ligament size distribution, this includes specifically details of the ligament morphology [78,79] and the size distribution of load-bearing rings in the ligament network [80]. Each of these parameters may impact the mechanical performance of LMD Nb, yet scaling laws that might be combined with our data for an informed discussion of that impact remain to be established.

5. Conclusions

This work investigates the microstructure and the mechanical behavior of millimeter-sized nanoporous (NP) Nb. Compared to aqueous dealloyed NP Au with similar φ as a benchmark, Young's modulus is found substantially lower. The reduced microstructural connectivity in NP Nb is consistent with its low stiffness. Yet, we conclude that this effect, on its own, is not sufficient and that additional factors contribute. The substantial increase in the coefficient of ligament size variation during coarsening appears significant, suggesting a less ordered evolution of porosity in NP Nb compared to aqueous dealloyed network materials such as NP Au.

Disclosure statement

No potential conflict of interest was reported by the author(s).

Funding

This work was supported by the Deutsche Forschungsgemeinschaft (DFG) within the Collaborative Research Centre SFB 986 'Tailor-Made MultiScale Materials Systems' (Project No. 192346071).

References

[1] Greer JR, Deshpande VS. Three-dimensional architected materials and structures: design, fabrication, and

mechanical behavior. MRS Bull. 2019;44:750–757. doi: 10.1557/mrs.2019.232
[2] Shi S, Li Y, Ngo-Dinh B-N, et al. Scaling behavior of stiffness and strength of hierarchical network nanomaterials. Science. 2021;371:1026–1033. doi: 10.1126/science.abd9391
[3] Ding Y, Chen MW. Nanoporous metals for catalytic and optical applications. MRS Bull. 2009;34:569–576. doi: 10.1557/mrs2009.156
[4] Wittstock G, Bäumer M, Dononelli W, et al. Nanoporous gold: from structure evolution to functional properties in catalysis and electrochemistry. Chem Rev. 2023;123:6716–6792. doi: 10.1021/acs.chemrev.2c00751
[5] Zhang J, Bai Q, Zhang Z. Dealloying-driven nanoporous palladium with superior electrochemical actuation performance. Nanoscale. 2016;8:7287–95. doi: 10.1039/C6NR00427J
[6] Shi S, Markmann J, Weissmüller J. Actuation by hydrogen electrosorption in hierarchical nanoporous palladium. Philos Mag. 2017;97:1571–1587. doi: 10.1080/14786435.2017.1311428
[7] Jin H-J, Wang X-L, Parida S, et al. Nanoporous Au- Pt alloys as large strain electrochemical actuators. Nano Lett. 2010;10:187–194. doi: 10.1021/nl903262b
[8] Dietrich L, Oppermann H, Lopper C, et al. Fabrication and characterization of nanoporous gold (NPG) interconnects for wafer level packaging. In: 2022 IEEE 72nd Electronic Components and Technology Conference (ECTC). p 873–882.
[9] Kucheyev SO, Hayes JR, Biener J, et al. Surface-enhanced Raman scattering on nanoporous Au. Appl Phys Lett. 2006;89:053102. doi: 10.1063/1.2260828
[10] Qian LH, Yan XQ, Fujita T, et al. Surface enhanced Raman scattering of nanoporous gold: smaller pore sizes stronger enhancements. Appl Phys Lett. 2007;90:153120. doi: 10.1063/1.2722199
[11] Seker E, Shih W-C, Stine KJ. Nanoporous metals by alloy corrosion: bioanalytical and biomedical applications. MRS Bull. 2018;43:49–56. doi: 10.1557/mrs.2017.298
[12] Stenner C, Shao L-H, Mameka N, et al. Piezoelectric gold: strong charge-load response in a metal-based hybrid nanomaterial. Adv Funct Mater. 2016;26:5174–5181. doi: 10.1002/adfm.v26.28
[13] Jin H-J, Weissmüller J. A material with electrically tunable strength and flow stress. Science. 2011;332:1179–1182. doi: 10.1126/science.1202190
[14] Bringa EM, Monk J, Caro A, et al. Are nanoporous materials radiation resistant? Nano Lett. 2012;12:3351–3355. doi: 10.1021/nl201383u
[15] Li R, Sieradzki K. Ductile-Brittle transition in random porous Au. Phys Rev Lett. 1992;68:1168–1171. doi: 10.1103/PhysRevLett.68.1168
[16] Senior NA, Newman RC. Synthesis of tough nanoporous metals by controlled electrolytic dealloying. Nanotechnology. 2006;17:2311–2316. doi: 10.1088/0957-4484/17/9/040
[17] Jin H-J, Kurmanaeva L, Schmauch J, et al. Deforming nanoporous metal: role of lattice coherency. Acta Mater. 2009;57:2665–2672. doi: 10.1016/j.actamat.2009.02.017
[18] Briot NJ, Kennerknecht T, Eberl C, et al. Mechanical properties of bulk single crystalline nanoporous gold investigated by millimetre-scale tension and compression testing. Philos Mag. 2014;94:847–866. doi: 10.1080/14786435.2013.868944
[19] Badwe N, Chen X, Sieradzki K. Mechanical properties of nanoporous gold in tension. Acta Mater. 2017;129:251–258. doi: 10.1016/j.actamat.2017.02.040
[20] Zandersons B, Lührs L, Li Y, et al. On factors defining the mechanical behavior of nanoporous gold. Acta Mater. 2021;215:116979. doi: 10.1016/j.actamat.2021.116979
[21] Volkert C, Lilleodden E, Kramer D, et al. Approaching the theoretical strength in nanoporous Au. Appl Phys Lett. 2006;89:061920. doi: 10.1063/1.2240109
[22] Liu R, Antoniou A. A relationship between the geometrical structure of a nanoporous metal foam and its modulus. Acta Mater. 2013;61:2390–2402. doi: 10.1016/j.actamat.2013.01.011
[23] Briot NJ, Balk TJ. Developing scaling relations for the yield strength of nanoporous gold. Philos Mag. 2015;95:2955–2973. doi: 10.1080/14786435.2015.1078512
[24] Jeon H, Lee S, Kim J-Y. Tension-compression asymmetry in plasticity of nanoporous gold. Acta Mater. 2020;199:340–351. doi: 10.1016/j.actamat.2020.08.054
[25] Wu Y, Markmann J, Lilleodden ET. On the consequences of intrinsic and extrinsic size effects on the mechanical response of nanoporous Au. Mater Des. 2023;232:112175. doi: 10.1016/j.matdes.2023.112175
[26] Erlebacher J, Aziz MJ, Karma A, et al. Evolution of nanoporosity in dealloying. Nature. 2001;410:450–453. doi: 10.1038/35068529
[27] Detsi E, Selles MS, Onck PR, et al. Nanoporous silver as electrochemical actuator. Scr Mater. 2013;69:195–198. doi: 10.1016/j.scriptamat.2013.04.003
[28] Wang C, Chen Q. Reduction-induced decomposition: spontaneous formation of monolithic nanoporous metals of tunable structural hierarchy and porosity. Chem Mater. 2018;30:3894–3900. doi: 10.1021/acs.chemmater.8b01431
[29] Jin H-J, Kramer D, Ivanisenko Y, et al. Macroscopically strong nanoporous Pt prepared by dealloying. Adv Eng Mater. 2007;9:849–854. doi: 10.1002/adem.v9:10
[30] Harrison JD, Wagner C. The attack of solid alloys by liquid metals and salt melts. Acta Metallurgica. 1959;7:722–735. doi: 10.1016/0001-6160(59)90178-6
[31] Wada T, Yubuta K, Inoue A, et al. Dealloying by metallic melt. Mater Lett. 2011;65:1076–1078. doi: 10.1016/j.matlet.2011.01.054
[32] Okulov I, Weissmüller J, Markmann J. Dealloying-based interpenetrating-phase nanocomposites matching the elastic behavior of human bone. Sci Rep. 2017;7:1–7. doi: 10.1038/s41598-017-00048-4
[33] Berger SA, Okulov IV. Open porous $\alpha + \beta$ titanium alloy by liquid metal dealloying for biomedical applications. Metals. 2020;10:1450. doi: 10.3390/met10111450
[34] Xiang Y-H, Liu L-Z, Shao J-C, et al. A universal scaling relationship between the strength and Young's modulus of dealloyed porous Fe0. 80Cr0. 20. Acta Mater. 2020;186:105–115. doi: 10.1016/j.actamat.2019.12.046
[35] Mokhtari M, Wada T, Le Bourlot C, et al. Low cost high specific surface architectured nanoporous metal

with corrosion resistance produced by liquid metal dealloying from commercial nickel superalloy. Scr Mater. 2019;163:5–8. doi: 10.1016/j.scriptamat.2018.12.023
[36] Kim JW, Wada T, Kim SG, et al. Enlarging the surface area of an electrolytic capacitor of porous niobium by MgCe eutectic liquid dealloying. Scr Mater. 2016;122:68–71. doi: 10.1016/j.scriptamat.2016.05.014
[37] Zhao C, Wada T, De Andrade V, et al. Three-dimensional morphological and chemical evolution of nanoporous stainless steel by liquid metal dealloying. ACS Appl Mater Interfaces. 2017;9:34172–34184. doi: 10.1021/acsami.7b04659
[38] Okulov AV, Joo S-H, Kim HS, et al. Nanoporous high-entropy alloy by liquid metal dealloying. Metals. 2020;10:1396. doi: 10.3390/met10101396
[39] Geslin P-A, McCue I, Gaskey B, et al. Topology-generating interfacial pattern formation during liquid metal dealloying. Nat Commun. 2015;6:1–8. doi: 10.1038/ncomms9887
[40] McCue I, Gaskey B, Geslin P-A, et al. Kinetics and morphological evolution of liquid metal dealloying. Acta Mater. 2016;115:10–23. doi: 10.1016/j.actamat.2016.05.032
[41] McCue I, Karma A, Erlebacher J. Pattern formation during electrochemical and liquid metal dealloying. Mrs Bull. 2018;43:27–34. doi: 10.1557/mrs.2017.301
[42] Chen-Wiegart Y-CK, Wada T, Butakov N, et al. 3D morphological evolution of porous titanium by X-ray micro- and nano-tomography. J Mater Res. 2013;28:2444–2452. doi: 10.1557/jmr.2013.151
[43] Liu L-Z, Ye X-L, Jin H-J. Interpreting anomalous low-strength and low-stiffness of nanoporous gold: quantification of network connectivity. Acta Mater. 2016;118:77–87. doi: 10.1016/j.actamat.2016.07.033
[44] Zednicek T, Vrana B, Millman W, et al. Tantalum and niobium technology roadmap. In: CARTS-Conference; 2002. p 142–147.
[45] Kim JW, Tsuda M, Wada T, et al. Optimizing niobium dealloying with metallic melt to fabricate porous structure for electrolytic capacitors. Acta Mater. 2015;84:497–505. doi: 10.1016/j.actamat.2014.11.002
[46] Stuckner J, Frei K, McCue I, et al. AQUAMI: an open source Python package and GUI for the automatic quantitative analysis of morphologically complex multiphase materials. Comput Mater Sci. 2017;139:320–329. doi: 10.1016/j.commatsci.2017.08.012
[47] Bapari S, Lührs L, Weissmüller J. Metrics for the characteristic length scale in the random bicontinuous microstructure of nanoporous gold. Acta Mater. 2023;260:119333. doi: 10.1016/j.actamat.2023.119333
[48] Hu K, Ziehmer M, Wang K, et al. Nanoporous gold: 3D structural analyses of representative volumes and their implications on scaling relations of mechanical behaviour. Philos Mag. 2016;96:3322–3335. doi: 10.1080/14786435.2016.1222087
[49] Schneider CA, Rasband WS, Eliceiri KW. NIH image to ImageJ: 25 years of image analysis. Nat Methods. 2012;9:671–675. doi: 10.1038/nmeth.2089
[50] Ostu N. A threshold selection method from gray-level histograms. IEEE Trans SMC. 1979;9:62.
[51] Doube M, Kłosowski MM, Arganda-Carreras I, et al. BoneJ: free and extensible bone image analysis in ImageJ. Bone. 2010;47:1076–1079. doi: 10.1016/j.bone.2010.08.023
[52] Odgaard A, Gundersen H. Quantification of connectivity in cancellous bone, with special emphasis on 3-D reconstructions. Bone. 1993;14:173–182. doi: 10.1016/8756-3282(93)90245-6
[53] Toriwaki J, Yonekura T. Euler number and connectivity indexes of a three dimensional digital picture. Forma-Tokyo-. 2002;17:183–209.
[54] Soyarslan C, Bargmann S, Pradas M, et al. 3D stochastic bicontinuous microstructures: generation, topology and elasticity. Acta Mater. 2018;149:326–340. doi: 10.1016/j.actamat.2018.01.005
[55] Grundner M, Halbritter J. XPS and AES studies on oxide growth and oxide coatings on niobium. J Appl Phys. 1980;51:397–405. doi: 10.1063/1.327386
[56] Ross RB. Metallic materials specification handbook. London: Springer Science & Business Media; 2013.
[57] Biener J, Hodge AM, Hamza AV, et al. Nanoporous Au: a high yield strength material. J Appl Phys. 2005;97:024301. doi: 10.1063/1.1832742
[58] Balk TJ, Eberl C, Sun Y, et al. Tensile and compressive microspecimen testing of bulk nanoporous gold. Jom. 2009;61:26–31. doi: 10.1007/s11837-009-0176-6
[59] Hodge A, Doucette R, Biener M, et al. Ag effects on the elastic modulus values of nanoporous Au foams. J Mater Res. 2009;24:1600–1606. doi: 10.1557/jmr.2009.0184
[60] Bürckert M, Briot NJ, Balk TJ. Uniaxial compression testing of bulk nanoporous gold. Philos Mag. 2017;97:1157–1178. doi: 10.1080/14786435.2017.1292060
[61] Mameka N, Wang K, Markmann J, et al. Nanoporous gold—testing macro-scale samples to probe small-scale mechanical behavior. Mater Res Lett. 2016;4:27–36. doi: 10.1080/21663831.2015.1094679
[62] Gibson I, Ashby MF. The mechanics of three-dimensional cellular materials. Proc R Soc Lond Ser A Math Phys Sci. 1982;382:43–59.
[63] Joo S-H, Jeong Y, Wada T, et al. Inhomogeneous dealloying kinetics along grain boundaries during liquid metal dealloying. J Mater Sci Technol. 2022;106:41–48. doi: 10.1016/j.jmst.2021.07.023
[64] Li Y, Ngô B-ND, Markmann J, et al. Topology evolution during coarsening of nanoscale metal network structures. Phys Rev Materials. 2019;3:076001. doi: 10.1103/PhysRevMaterials.3.076001
[65] Ye X-L, Lu N, Li X-J, et al. Primary and secondary dealloying of Au(Pt)-Ag: structural and compositional evolutions, and volume shrinkage. J Electrochem Soc. 2014;161:C517–C526. doi: 10.1149/2.0131412jes
[66] Li Y, Ngo-Dinh B-N, Markmann J, et al. Evolution of length scales and of chemical heterogeneity during primary and secondary dealloying. Acta Mater. 2022;222:117424. doi: 10.1016/j.actamat.2021.117424
[67] Shi S, Markmann J, Weissmüller J. Synthesis of uniform bulk nanoporous palladium with tunable structure. Electrochim Acta. 2018;285:60–69. doi: 10.1016/j.electacta.2018.07.081
[68] Lai L, Gaskey B, Chuang A, et al. Topological control of liquid-metal-dealloyed structures. Nat Commun. 2022;13:1–10.

[69] Erlebacher J. Mechanism of coarsening and bubble formation in high-genus nanoporous metals. Phys Rev Lett. 2011;106:225504. doi: 10.1103/PhysRevLett.106.225504
[70] Elsner BA, Müller S, Bargmann S, et al. Surface excess elasticity of gold: Ab initio coefficients and impact on the effective elastic response of nanowires. Acta Mater. 2017;124:468–477. doi: 10.1016/j.actamat.2016.10.066
[71] Jin H-J, Weissmüller J, Farkas D. Mechanical response of nanoporous metals: a story of size, surface stress, and severed struts. Mrs Bull. 2018;43:35–42. doi: 10.1557/mrs.2017.302
[72] Mangipudi K, Epler E, Volkert C. Topology-dependent scaling laws for the stiffness and strength of nanoporous gold. Acta Mater. 2016;119:115–122. doi: 10.1016/j.actamat.2016.08.012
[73] Biener J, Hodge AM, Hayes JR, et al. Size effects on the mechanical behavior of nanoporous Au. Nano Lett. 2006;6:2379–2382. doi: 10.1021/nl061978i
[74] Sun X-Y, Xu G-K, Li X, et al. Mechanical properties and scaling laws of nanoporous gold. J Appl Phys. 2013;113:023505. doi: 10.1063/1.4774246
[75] Huber N, Viswanath R, Mameka N, et al. Scaling laws of nanoporous metals under uniaxial compression. Acta Mater. 2014;67:252–265. doi: 10.1016/j.actamat.2013.12.003
[76] Huber N. Connections between topology and macroscopic mechanical properties of three-dimensional open-pore materials. Front Mater. 2018;5:69. doi: 10.3389/fmats.2018.00069
[77] Sohn S, Richert C, Shi S, et al. Scaling between elasticity and topological genus for random network nanomaterials. Extreme Mech Lett. 2024;68:102147. doi: 10.1016/j.eml.2024.102147
[78] Richert C, Huber N. Skeletonization, geometrical analysis, and finite element modeling of nanoporous gold based on 3D tomography data. Metals. 2018;8:282. doi: 10.3390/met8040282
[79] Zou L, Shao J-C, Jin H-J. Ligament morphology and elastic modulus of porous structure formed by liquid metal dealloying. J Mater Res Technol. 2024;31:3914–3920. doi: 10.1016/j.jmrt.2024.07.091
[80] Ziehmer M, Lilleodden ET. The isothermal evolution of nanoporous gold from the ring perspective—an application of graph theory. Acta Mater. 2020;199:669–679. doi: 10.1016/j.actamat.2020.08.026